RESUME: Turning an SWI acquisition into a fast qMRI protocol

Serena Monti[1], Pasquale Borrelli[1], Enrico Tedeschi[2], Sirio Cocozza[2], Giuseppe Palma[3]*

1 IRCCS SDN, Naples, Italy, **2** Department of Advanced Biomedical Sciences, University "Federico II", Naples, Italy, **3** Institute of Biostructures and Bioimaging, National Research Council, Naples, Italy

* giuseppe.palma@ibb.cnr.it

Abstract

Susceptibility Weighted Imaging (SWI) is a common MRI technique that exploits the magnetic susceptibility differences between the tissues to provide valuable image contrasts, both in research and clinical contexts. However, despite its increased clinical use, SWI is not intrinsically suitable for quantitation purposes. Conversely, quantitative Magnetic Resonance Imaging (qMRI) provides a way to disentangle the sources of common MR image contrasts (*e.g.* proton density, T_1, etc.) and to measure physical parameters intrinsically related to tissue microstructure. Unfortunately, the poor signal-to-noise ratio and resolution, coupled with the long imaging time of most qMRI strategies, have hindered the integration of quantitative imaging into clinical protocols. Here we present the RElaxometry and SUsceptibility Mapping Expedient (RESUME) to show that the standard acquisition leading to a clinical SWI dataset can be easily turned into a thorough qMRI protocol at the cost of a further 50% of the SWI scan time. The R_1, R_2^*, proton density and magnetic susceptibility maps provided by the RESUME scheme alongside the SWI reconstruction exhibit high reproducibility and accuracy, and a submillimeter resolution is proven to be compatible with a total scan time of 7 minutes.

Introduction

In the last two decades Susceptibility Weighted Imaging (SWI) [1] has been increasingly used in neuroimaging MRI protocols, owing to its ability to detect the presence of paramagnetic (deoxyhaemoglobin, haemosiderin, ferritin, etc.) or diamagnetic (calcium hydroxyapatite or apatitelike minerals, myelin, oxyhaemoglobin, etc.) compounds [2–5].

Numerous studies have demonstrated the clinical relevance of this technique across a wide range of pathological conditions [6], including neuroinflammation, neurodegeneration and head trauma. Moreover, it is valuable in the detection of cerebral micro-bleeds in aging population, in the follow-up of hemorrhagic infarctions, and in the assessment of cavernous malformations, venous thrombosis, and calcium or iron deposition, as thoroughly reviewed in [7–9].

Although several MRI Gradient Echo (GRE) signals (Steady-State Free-Precession—SSFP [10], Echo-Shifted—ES [11], etc.) acquired with different spatial encoding strategies

(Projection Acquisition—PA [12], Periodically Rotated Overlapping ParallEL Lines with Enhanced Reconstruction—PROPELLER [13], Echo Planar Imaging—EPI [14], etc.) can be processed to obtain an SWI dataset, it is common practice to rely on a standard 3D single spoiled GRE with a relatively long echo time (usually $T_E \sim 20$ ms at 3 T [15]). Such choice, however, seems suboptimal, as at least one more echo at short T_E could fit within an otherwise dead-time of the sequence. Indeed, even at moderately low receiver bandwidths (BW of the order of 100 Hz/pixel), the sampling time of an echo $t_s = 1/\text{BW}$ is of the order of 10 ms, thus allowing for the acquisition of one more signal at $T_E \sim 8$ ms. The rationale behind the acquisition of more echoes should not be found in their availability without inducing major changes that may alter the original GRE signal at long T_E (in terms of contrast, SNR, etc.). Indeed, multi-echo GRE allows for R_2^* quantification [16], along with a more accurate estimate of Quantitative Susceptibility Mapping (QSM) compared to what obtained with the single-echo acquisition [17]. These quantitative parameters provide a robust and comprehensive characterization of the tissue susceptibility, which may shed light in many areas of clinical interest (from mineral metabolism [18] to vein segmentation [19, 20]).

On the other hand, a more thorough approach to quantitative MRI (qMRI) is desirable in a wide spectrum of clinical conditions [21], since R_1 and Proton Density (PD) give complementary and more detailed information on water tissue content. These parameters were shown to provide unique insights into the status of white matter in normal aging and demyelinating disease [22–24] or into tumor characterization [25, 26]. In [27], PD was used to derive Macromolecular Tissue Volume Fraction (MTVF) maps, which provide a sensitive measure of the disease status in multiple sclerosis patients, and, together with R_1 maps, allow for an estimation of the apparent volume of interacting water protons (strictly related to the properties of local physico-chemical environment). Moreover, R_1, coupled to R_2^*, is a key to determine the stage of haemorrhages [28] or to obtain absolute measures of contrast agent concentrations within tissues [29, 30]. In addition, the joint availability of R_1, R_2^* and susceptibility measures in Fabry's disease has been recently exploited to redefine the pathogenetic mechanisms and the incidence of the pulvinar sign in that metabolic disorder [31].

R_1 and PD maps are usually derived from two or more spoiled GRE sequences acquired at fixed T_R and variable Flip Angle (FA) [32]. Therefore, one may consider to append one more GRE sequence (*e.g.* with a lower FA) to that used for SWI, QSM and R_2^* mapping [16]. However, an unpleasant and straightforward consequence of R_1 mapping by variable FAs consists in the increased total acquisition time, which clearly doubles the original duration of the SWI protocol, and certainly limits its clinical applicability.

Here we present the RElaxometry and SUsceptibility Mapping Expedient (RESUME) that halves the duration of the supplementary acquisition, still providing the complete set of qMRI maps (R_1, R_2^*, PD and QSM) along with the SWI processing.

Materials and methods

RESUME is a qMRI scheme consisting of a 3D acquisition protocol coupled with the analytical solution of the Bloch equations associated to the acquired MRI signals. The protocol is derived from a standard SWI acquisition, modified to sample at least two echoes, and by the addition of one more spoiled GRE sequence with halved repetition time.

First, the analytical solution of the qMRI problem is given for a single-echo spoiled GRE (with repetition time $T_{R,0}$, echo time $T_{E,0}$ and FA θ_1) and a multi-echo spoiled GRE (with repetition time $2 \cdot T_{R,0}$, echo times $\{T_{E,i}\}$ and FA θ_2). Finally, more details on the actual acquisition setup will be given.

Analytical solution of the qMRI equations

Spoiled GRE signal.   The complex signal of a spoiled GRE sequence is

$$S = K \cdot M_0 \cdot \sin \theta \cdot \frac{1 - E_1}{1 - E_1 \cos \theta} \cdot e^{-T_E \cdot (R_2^* + i\gamma_n \Delta B) + i\phi_0} \ , \tag{1}$$

where K is the complex coil sensitivity, M_0 is the equilibrium magnetization, $E_1 \equiv \exp(-T_R \cdot R_1)$, γ_n is the gyromagnetic ratio of the imaged nucleus, ΔB is the local magnetic field variation and ϕ_0 is the phase-shift induced by the RF-pulse [16].

R_2^* map.   If s_i represents the magnitude of the i-th echo of the multi-echo spoiled GRE, from Eq 1 it follows that

$$\log s_i = k_0 - T_{E,i} \cdot R_2^* \tag{2}$$

for

$$k_0 = \log \left[|K| \cdot M_0 \cdot \sin \theta_2 \cdot \frac{1 - E_1}{1 - E_1 \cos \theta_2} \right] \ . \tag{3}$$

Therefore, a simple regression via weighted least squares leads to the following estimates of

$$R_2^* = -\frac{\sum_{i=1}^{n} w_i (T_{E,i} - \overline{T}_E)(\log s_i - \overline{L})}{\sum_{i=1}^{n} w_i (T_{E,i} - \overline{T}_E)^2} \tag{4}$$

and

$$k_0 = \overline{L} + R_2^* \cdot \overline{T}_E \ , \tag{5}$$

where

$$\overline{T}_E = \frac{\sum_{i=1}^{n} w_i T_{E,i}}{\sum_{i=1}^{n} w_i} \ , \qquad \overline{L} = \frac{\sum_{i=1}^{n} w_i \log s_i}{\sum_{i=1}^{n} w_i} \ , \quad \text{and} \quad w_i = \frac{1}{\text{BW}_i \cdot s_i^2} \ . \tag{6}$$

Eq 4 reduces to

$$R_2^* = \frac{\log (s_1/s_2)}{T_{E,2} - T_{E,1}} \tag{7}$$

in case of double-echo acquisitions.

R_1 map.   Eqs 1, 4 and 5 allow the estimation of the signal magnitude at $T_E = 0$ of the single-echo (S_1) and multi-echo (S_2) spoiled GREs as

$$S_1 = s_0 \cdot e^{T_{E,0} \cdot R_2^*} \tag{8}$$

(s_0 being the magnitude of the single-echo GRE) and

$$S_2 = e^{k_0} \tag{9}$$

(see Eq 3).

On the other hand,

$$S_1 = |K| \cdot M_0 \cdot \sin \theta_1 \cdot \frac{1 - E_{1,0}}{1 - E_{1,0} \cos \theta_1} \tag{10}$$

and

$$S_2 = |K| \cdot M_0 \cdot \sin \theta_2 \cdot \frac{1 - E_{1,0}^2}{1 - E_{1,0}^2 \cos \theta_2} \quad , \tag{11}$$

where $E_{1,0} \equiv \exp(-T_{R,0} \cdot R_1)$.

Therefore, defining

$$q = S_1 / S_2 \tag{12}$$

and

$$k = \frac{\sin \theta_1}{\sin \theta_2} \quad , \tag{13}$$

from Eqs 10 and 11 it comes out that

$$q = \frac{k(1 - E_{1,0}^2 \cos \theta_2)}{(1 + E_{1,0})(1 - E_{1,0} \cos \theta_1)} \quad . \tag{14}$$

Solving with respect to $E_{1,0}$, two solutions are found:

$$E_{1,0}^{\pm} = \frac{R \pm \sqrt{R^2 + 4C(q - k)}}{2C} \quad , \tag{15}$$

where

$$R = q(1 - \cos \theta_1) \tag{16}$$

and

$$C = q \cos \theta_1 - k \cos \theta_2 \quad . \tag{17}$$

Unfortunately, for some pairs (θ_1, θ_2) both solutions in Eq 15 may satisfy $0 < E_{1,0} < 1$ (see Fig 1a)), thus precluding the possibility to find an unambiguous R_1 value for each $(\theta_1, \theta_2, S_1, S_2)$.

In order to determine which of the solutions in Eq 15 is physically relevant, $E_{1,0}^{+}$ is recognized as

$$E_{1,0}^{+} = E_{1,0}^{+}[\theta_1, \theta_2, S_1(E_{1,0}, \theta_1), S_2(E_{1,0}, \theta_2)] = f[\theta_1, \theta_2, E_{1,0}] \quad . \tag{18}$$

Looking for the parametric domain in which the condition

$$f[\theta_1, \theta_2, E_{1,0}] = E_{1,0} \tag{19}$$

is satisfied, after some algebraic manipulation, it results that:

$$E_{1,0} = \begin{cases} E_{1,0}^{+} & \text{if } \cos \theta_1 \geq \dfrac{1 + \cos \theta_2 \cdot E_{1,0}(2 + E_{1,0})}{1 + E_{1,0}(2 + \cos \theta_2 \cdot E_{1,0})} \\[12pt] E_{1,0}^{-} & \text{otherwise.} \end{cases} \quad ; \tag{20}$$

Of note, the condition in Eq 20 explicitly depends on the unknown $E_{1,0}$ (see Fig 1b)). However, the graphics in Fig 1c) and 1d) show that for $E_{1,0} > e^{-1}$ (corresponding to the realistic condition in which $T_{R,0} < T_1$), for any $0 < \theta_2 < \pi$ and $0 < \theta_1 < 0.47 \cdot \theta_2$, $E_{1,0}^{+}$ provides the
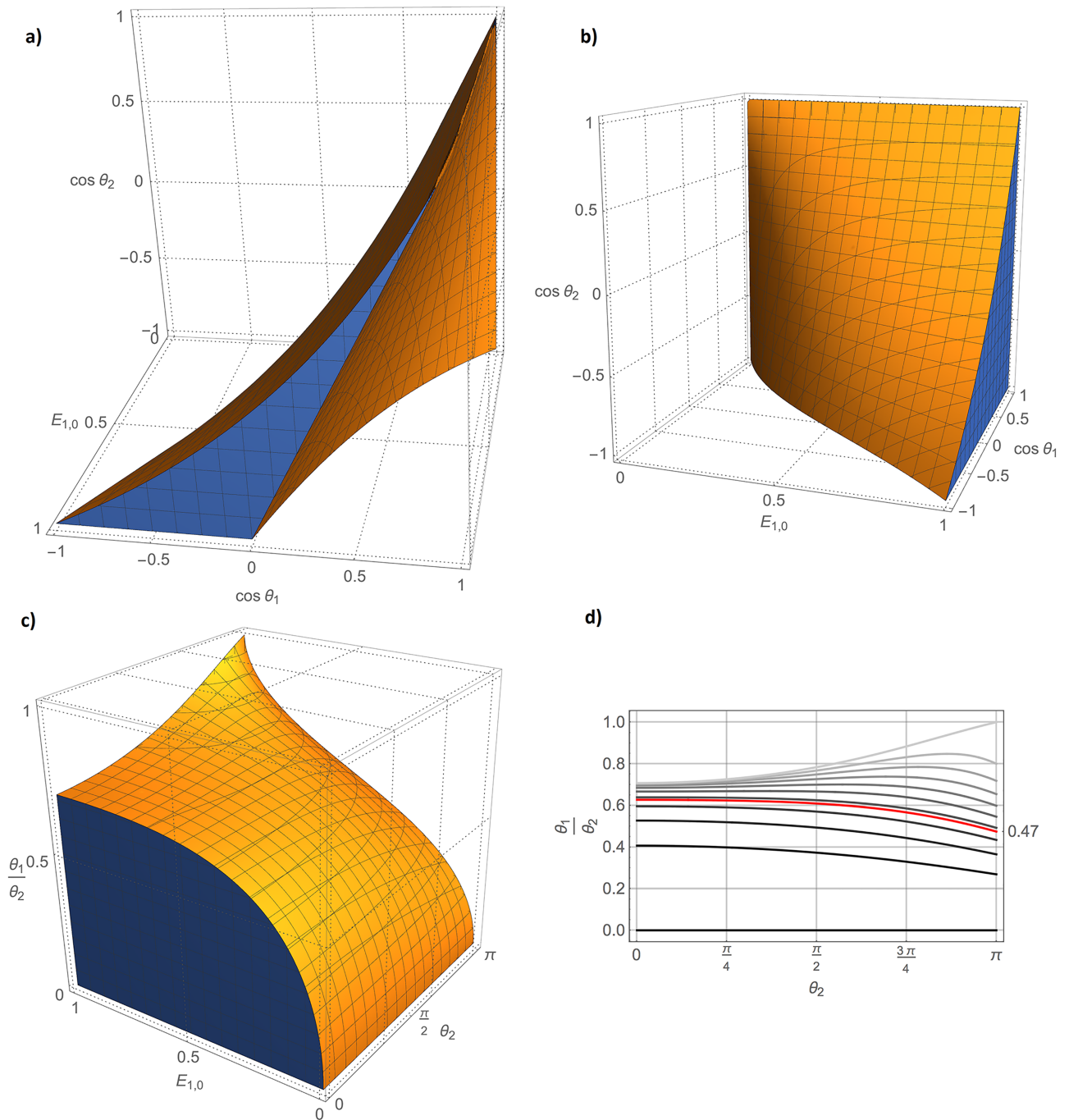
Fig 1. Numerical details about the analytical solutions $E_{1,0}^{\pm}$. a) Region in the parameter space ($\cos\theta_1$, $\cos\theta_2$, $E_{1,0}$) in which both solutions $E_{1,0}^{\pm}$ satisfy the physical constrain $0 < E_1 < 1$. b) Region in the parameter space ($\cos\theta_1$, $\cos\theta_2$, $E_{1,0}$) in which solution $E_{1,0}^{+}$ applies. c) Region in the parameter space (θ_1/θ_2, θ_2, $E_{1,0}$) in which solution $E_{1,0}^{+}$ applies. d) Family of curves parametrized by $E_{1,0}$ (ranging from 0 [black] to 1 [light gray] in step of 0.1) that pose an upper limit to θ_1/θ_2 for $E_{1,0}^{+}$ to be acceptable. The red curve corresponds to $E_{1,0} = e^{-1}$ and entirely lies in the half-plane $\theta_1/\theta_2 > 0.47$.

https://doi.org/10.1371/journal.pone.0189933.g001

correct solution to Eq 14. Therefore, in the following it will be assumed that

$$R_1 = -\frac{\log E_{1,0}^+}{T_R} \ .$$

(21)

A thorough analysis of the FAs θ_1 and θ_2 that optimize the R_1 map SNR in the general case of a multi-echo GRE with multiple echoes and variable BW_i is quite complex and, probably, not really insightful. However, in the specific case of a double-echo GRE acquired with $T_{E,1} = T_{E,0}$ and $BW_1 = BW_0$ (which is the most realistic condition—see the section dedicated to acquisition), a useful numerical approach can be adopted. From $BW_1 = BW_0$, it follows that S_1 and S_2 share the same noise power σ_S^2. Therefore the variance of the R_1 estimate can be expressed as

$$\sigma_{R_1}^2(\theta_1, \theta_2, R_1) = \left(\left\{ \frac{\partial E_{1,0}^+}{\partial S_1}[\theta_1, \theta_2, S_1(\theta_1, R_1), S_2(\theta_2, R_1)] \right\}^2 + \left\{ \frac{\partial E_{1,0}^+}{\partial S_2}[\theta_1, \theta_2, S_1(\theta_1, R_1), S_2(\theta_2, R_1)] \right\}^2 \right) \cdot \left[\frac{\sigma_S}{T_{R,0} \cdot E_{1,0}(R_1)} \right]^2 .$$

(22)

The optimal FAs $\bar\theta_1$ and $\bar\theta_2$ are thus obtained by minimizing $\sigma_{R_1}^2$ for a given R_1; the numerical results are shown for a wide range of practical $R_1 \cdot T_{R,0}$ in Fig 2.
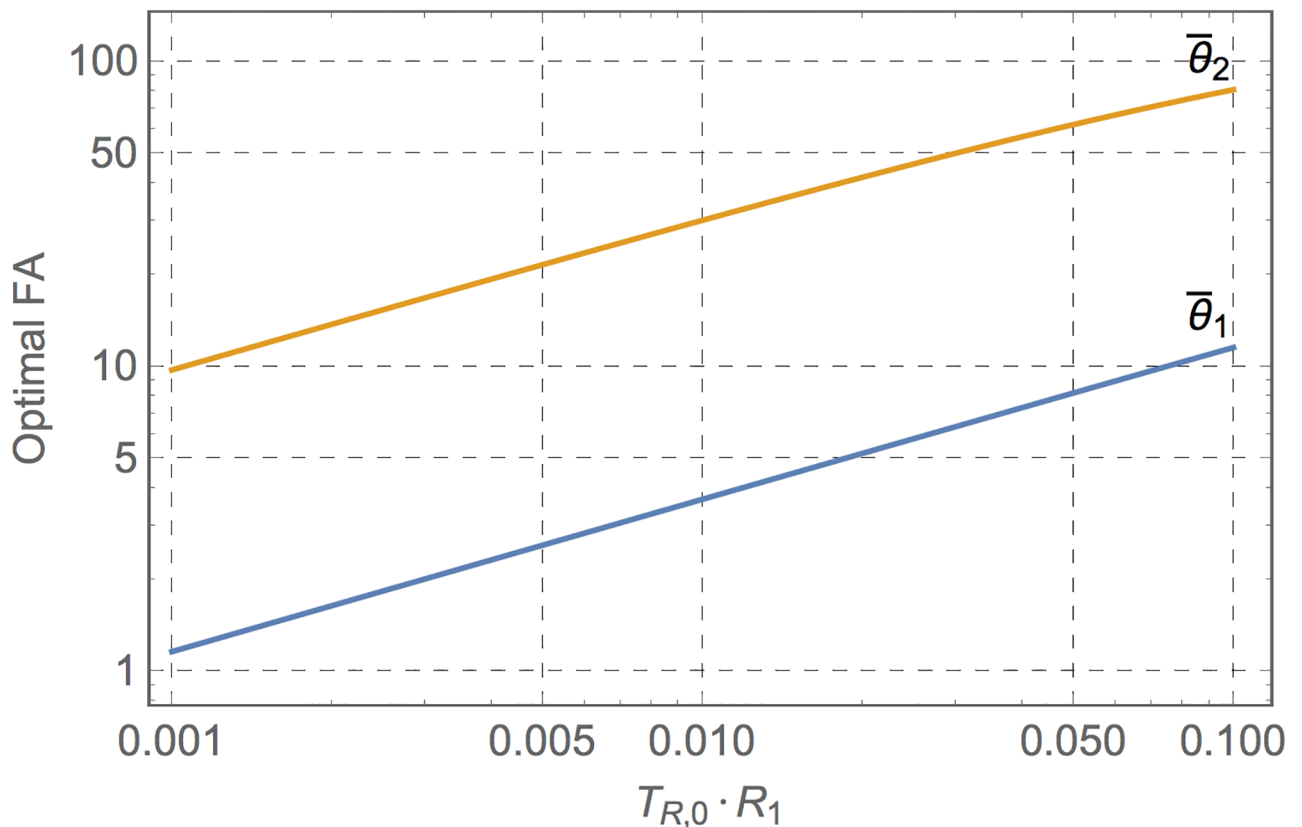
Fig 2. Optimal Flip Angles (FAs) for R_1 mapping. FAs $\bar\theta_1$ and $\bar\theta_2$ of single- and double-GRE sequences that maximize the accuracy of R_1 estimate as a function of the expected $T_{R,0} \cdot R_1$.

PD map. From Eq 11, PD can be estimated as

$$|K|M_0 = S_2 \cdot \frac{1 - E_{1,0}^2 \cos\theta_2}{\sin\theta_2 \cdot (1 - E_{1,0}^2)} \quad . \tag{23}$$

QSM. There are plenty of techniques that can be used to derive the QSM from the complex signal in Eq 1 (for a recent overview, see [33]), each more or less recommended depending on the specific application. A highly accurate reconstruction scheme is given by the algorithm introduced in [34], which is here adopted to obtain the map shown in the Results from the phase images of the multi-echo GRE sequences.

MRI acquisition

MRI was performed using a 3 T scanner (Trio, Siemens Medical Systems, Erlangen, Germany) with a volume transmitter coil and an 8-channel head receiver coil. Sequences were acquired after having obtained an informed consent for experimentation with human subjects. The "Carlo Romano" ethics committee for biomedical activities of "Federico II" University of Naples (Italy) specifically approved the study and the written informed consent form, which was signed by the subject undergoing the MR scan.

The 3D RESUME protocol actually acquired for this study consists of:

1. a single-echo flow-compensated spoiled GRE sequence (Repetition Time: T_R = 14 ms; Echo Time: T_{E1} = 7.63 ms; FA: θ_1 = 2˚);

2. a dual-echo flow-compensated spoiled GRE sequence (Repetition Time: $2 \cdot T_R$ = 28 ms; Echo Times: T_{E1} = 7.63 ms and T_{E2} = 22.14 ms; FA: θ_2 = 20˚).

Both sequences shared the same geometry (pseudo-axial orientation along the anterior commissure-posterior commissure; Field of View (FOV) = $230 \times 194 \times 166$ mm³; voxel size $\Delta V = 0.65 \times 0.65 \times 1.3$ mm³; GRAPPA acceleration factor = 2) and were acquired with a BW of 190 Hz/pixel in a total acquisition time of 7' 9". For each echo, a magnitude/phase reconstruction was enabled, thus obtaining a total of 3 complex volume datasets.

According to the chosen FAs, the SNR of the resulting R_1 map can be estimated from Eq 22. This quality index can be made independent from the noise power within the acquired images by normalizing it to the SNR of the input GRE images (possibly after some denoising) computed in an average brain parenchyma (with a nominal $T_{1,par}$ = 1 s). The result is shown in Fig 3 as a function of the expected T_1.

Denoising

Before computing the R_2^*, R_1 and PD maps according to Eqs 4, 21 and 23, the acquired datasets were denoised following a revised version of the Multi-spectral Non-Local Means (MNLM) approach first described in [16].

Briefly, in this context, M different datasets are considered as a multi-component image $X : \mathbb{R}^N \to \mathbb{R}^M$ ($N = 3$) with bounded support $\Omega \subset \mathbb{R}^N$. The MNLM is, then, a class of endomorphisms of the image space, each identified by 3 parameters (κ, ρ and ς), that act as follows:

$$[\text{MNLM}_{\kappa,\rho,\varsigma}(X)]_m(\vec{x}) = Y_m(\vec{x}) = \frac{\int_{B_r[\vec{x}]} W_m(\vec{x}, \vec{y}) X_m(\vec{y}) d\vec{y}}{\int_{B_r[\vec{x}]} W_m(\vec{x}, \vec{y}) d\vec{y}} . \tag{24}$$
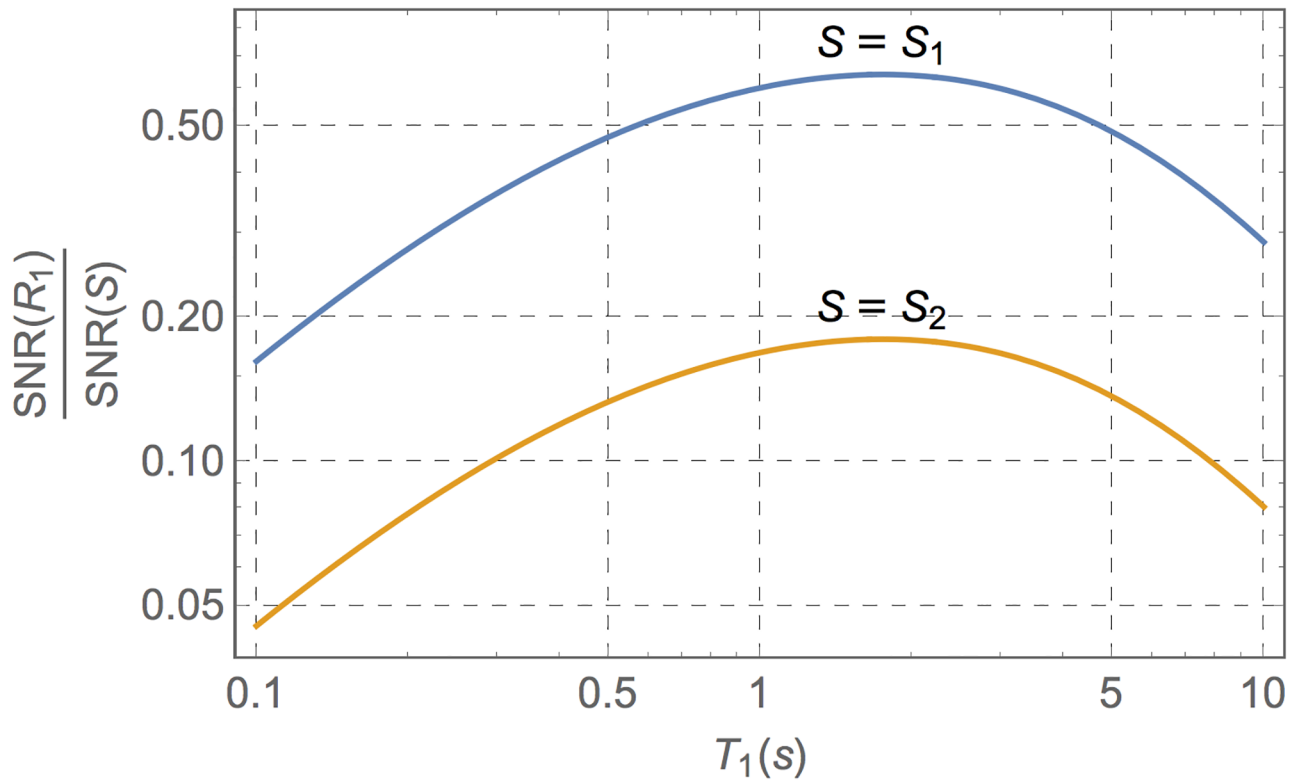
Fig 3. Ratio between the SNR of the estimated R_1 map and the SNR of the S images in an average brain parenchyma (with $T_{1,par}$ = 1 s) as a function of the expected T_1, for θ_1 = 2˚ and θ_2 = 20˚.

In [Eq 24](#) $B_r[\vec{x}]$ is the ball centered in $\vec{x}$, whose radius r is defined such that

$$\int_{B_r[\vec{x}]} W_m(\vec{x}, \vec{y})d\vec{y} = \kappa \ , \tag{25}$$

where

$$W_m(\vec{x}, \vec{y}) \equiv \exp\left[-\frac{d_\rho^2(\vec{x}, \vec{y})}{\varsigma^2} \cdot \frac{Q_m(\vec{x})}{\sum_{l=1}^M Q_l(\vec{x})}\right] , \tag{26}$$

$$d_\rho^2(\vec{x}, \vec{y}) \equiv \sum_{m=1}^M \left\{ \int_{\mathbb{R}^N} \frac{|X_m(\vec{x} + \vec{t}) - X_m(\vec{y} + \vec{t})|^2}{\sigma_m^2(\vec{x}) + \sigma_m^2(\vec{y})} \cdot \frac{\exp -\frac{\|\vec{t}\|^2}{2\rho^2}}{\left(\sqrt{2\pi} \cdot \rho\right)^N} d\vec{t} \right\}, \tag{27}$$

$$Q_m(\vec{x}) \equiv \frac{\int_\Omega X_m^2(\vec{y})d\vec{y}}{\int_\Omega \sigma_m^2(\vec{x})d\vec{y}} \ , \tag{28}$$

$\kappa \sim 10^2 \cdot \Delta V$ provides a criterion to dynamically allocate a search window, $\rho \sim \sqrt[N]{5 \cdot \Delta V}$ is the similarity radius, $\varsigma \sim 1$ is a dimensionless constant to be manually tuned that determines the filter strength, and $\sigma_m(\vec{x})$ is the standard deviation of noise of the mth image component at $\vec{x} \in \Omega$ (the noise power maps were estimated following [35]).

The denoising of the magnitude datasets (s_0, s_1 and s_2) required by R_2^*, R_1 and PD calculation was performed by exploiting also the information contained within the QSM derived from the phase images. Therefore, a total of $M = 4$ real datasets were jointly processed in Eq 24.

Due to the high computational complexity of the above scheme, a multi-Graphics Processing Unit (GPU) implementation of the MNLM algorithm [36] was adapted to Eq 24 and exploited for fast image processing.

Field inhomogeneity correction

B_1^+ non-ideal profiles critically influence the accuracy of the R_1 and PD estimates. In particular, while R_1 just depends only on B_1^+ through the presence of $\theta_{1,2}$ in Eq 15 (the receiver coil sensitivity B_1^- is eliminated in the ratio of signal intensities in Eq 12), PD is also affected by B_1^- via S_2 in Eq 23.

If a protocol for a fast measurement of B_1 profiles of slab-selective RF-pulses is available on the scanner, the actual B_1 maps can be directly used in Eqs 15 and 23 to obtain bias-free R_1 and PD maps.

In the results shown below, to get rid of such biases, the effective approach based on the information content of the derived maps proposed in [16] was adopted.

RESUME assessment

The reproducibility and the accuracy of the RESUME maps were estimated on a pool of 10 subjects (5 patients and 5 healthy controls—HCs—were recruited in order to test the method across a broad range of tissue parameters) by applying the following procedure on each of them (hereafter identified by the index $j = 1, \ldots, 10$).

First, to obtain the confidence interval of the RESUME maps, each sequence of the protocol was acquired twice during the same session. Given the redundant set of complex datasets, an ensemble of 2^3 (cardinality of the Cartesian product of magnitude datasets s_0, s_1 and s_2) $\times 2^2$ (cardinality of the Cartesian product of phase datasets from the dual-echo GRE—used for QSM) choices of different complete RESUME protocols was produced. Thirty-two different estimates of the relaxometry and susceptibility maps were thus derived and used to estimate the overall reproducibility (accounting for image uncorrelated noise, variations in signal amplification of the MR scanner, tissue temperature fluctuations, etc.) via voxelwise mean ($\boldsymbol{\mu}_j(\vec{x})$) and standard deviation ($\boldsymbol{\sigma}_j(\vec{x})$) maps.

Moreover, the RESUME R_1, R_2^* and PD maps were compared with the corresponding maps derived on the same subject using another qMRI approach established in [16]. This approach is based on two or more multi-echo spoiled 3D GRE sequences, in which all acquisition parameters are kept constant, except the FA, which is varied in order to provide different T_1-weights. The acquired signals are then conveniently combined in order to derive high SNR maps of R_1, R_2^*, PD and magnetic susceptibility.

On the other hand, the RESUME susceptibility map was compared to the QSM derived from an 8-echo GRE sequence (Repetition time: 28 ms; Echo Times: $\{T_{E,i} = [3.38 + (i-1) \cdot 2.82]$ ms$\}$; FA: 20˚; BW: 400 Hz/pixel), acquired with bipolar readout gradients (no flow-compensation) and the same geometry of the RESUME sequences.

The accuracy was finally evaluated via the difference magnitude ($\boldsymbol{\delta}_j(\vec{x})$) between RESUME maps and the maps used for comparison.

For evaluation purposes, a healthy control (HC1) was chosen as the common spatial reference for the pool of subjects. The reproducibility ($\{\boldsymbol{\sigma}_j(\vec{x}) \mid j = 2, \ldots, 10\}$) and accuracy

($\{\boldsymbol{\delta}_j(\vec{x}) \mid j = 2, \ldots, 10\}$) maps obtained for each other subject were, then, spatially normalized to HC1 according to the deformation field given by the elastic registration of the dual GRE image acquired at $T_{E,1}$ on the corresponding HC1 image. Furthermore, for a numerical assessment of the maps, the median values within the brain mask were extracted for each patient from $\{\boldsymbol{\sigma}_j(\vec{x})\}$ and $\{\boldsymbol{\delta}_j(\vec{x})\}$.

To compare the RESUME measures with the values found in the literature, an expert neuroradiologist manually drew a set of bilateral Regions of Interest (ROIs) on the R_1 map of HCs in the white matter, in the cortical grey matter, in the head of the caudate nucleus and in the putamen; the mean values of R_1, R_2^*, PD and QSM were then extracted for further comparisons.

Full access to the obtained results is provided at https://figshare.com/s/6d467faa11579c7c0c02.

Image processing

All data processing, except the QSM (which was obtained by the free tool described in [34]), was performed using an in-house developed library for Matlab (MATLAB® Release 2012b, The MathWorks, Inc., Natick, MA, USA), partly described in previous works [16, 35–37], on a commercial workstation (Intel® Core™ i7-3820 CPU @ 3.6 GHz; RAM 16 GB) equipped with 2 GPU boards (NVIDIA GeForce® GTX 690). The demonstrative application of qMRI for vein segmentation, and Oxygen Extraction Fraction (OEF) and MTVF mapping was respectively provided by the MAVEN algorithm [20] and the in-house implementations of the methods described in [27, 38].

Results

Each RESUME processing took 10 minutes on the above described workstation.

The derived maps exhibit a uniform quality throughout the entire FOV, and provide adequate spatial and contrast resolution for clear identification of the brain structures at different axial levels (see Fig 4). Moreover, the resolution of the acquired datasets allows for satisfactory multi-planar reconstructions (see Fig 5).

Reproducibility and accuracy measures of RESUME were available both for visual inspection (see Fig 6) and in terms of summarizing numerical indices. In particular, in the pool of the analyzed subjects, the median values of $\{\boldsymbol{\sigma}_j(\vec{x})\}$ within the brain mask were normalized to the range of the associated $\{\boldsymbol{\mu}_j(\vec{x})\}$ maps, and their mean values were $(1.38 \pm 0.19)\%$ for R_1 map, $(3.11 \pm 0.82)\%$ for R_2^* map, $(1.22 \pm 0.20)\%$ for PD map, and $(1.43 \pm 0.15)\%$ for QSM. Similarly, the averages over the normalized median values of $\{\boldsymbol{\delta}_j(\vec{x})\}$ were $(1.38 \pm 0.17)\%$ for R_1 map, $(2.15 \pm 0.59)\%$ for R_2^* map, $(1.17 \pm 0.15)\%$ for PD map, and $(1.83 \pm 0.23)\%$ for QSM.

The RESUME values measured in the ROIs manually drawn in different brain structures of the HCs largely overlap with the corresponding ranges derived from the reference method [16] in the same cohort of subjects or found in the literature for different groups of HCs (see Table 1).

The output of an extended quantitative processing entirely based on the RESUME protocol is shown in Fig 7, where R_1, R_2^*, PD and QSM come along with the MAVEN vein segmentation, the OEF and MTVF maps.

Discussion

The search of quantitative and reproducible measures in MRI is of unquestionable interest for the scientific community. Indeed, qMRI methods directly focus on physical and objective
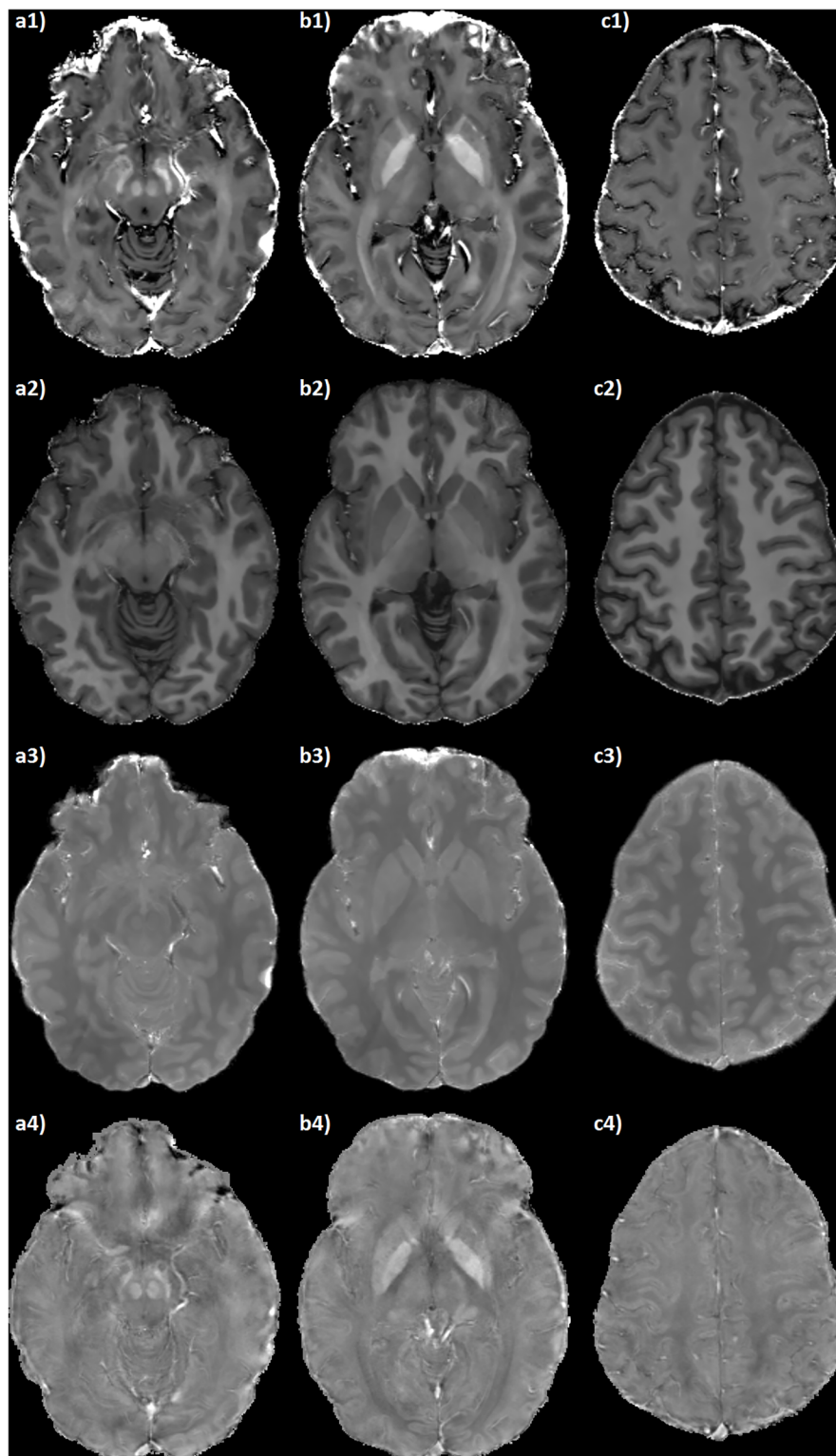
Fig 4. Axial RESUME maps of the brain. Slices at the level of midbrain (a), basal ganglia (b) and centra semiovalia (c) of: 1) R_2^* map ([0 ∼ 50] s^{-1}); 2) R_1 map ([0 ∼ 2] s^{-1}); 3) PD map ([0 ∼ 1] arbitrary units); 4) QSM ([−300 ∼ 300] · 10^{-9}).
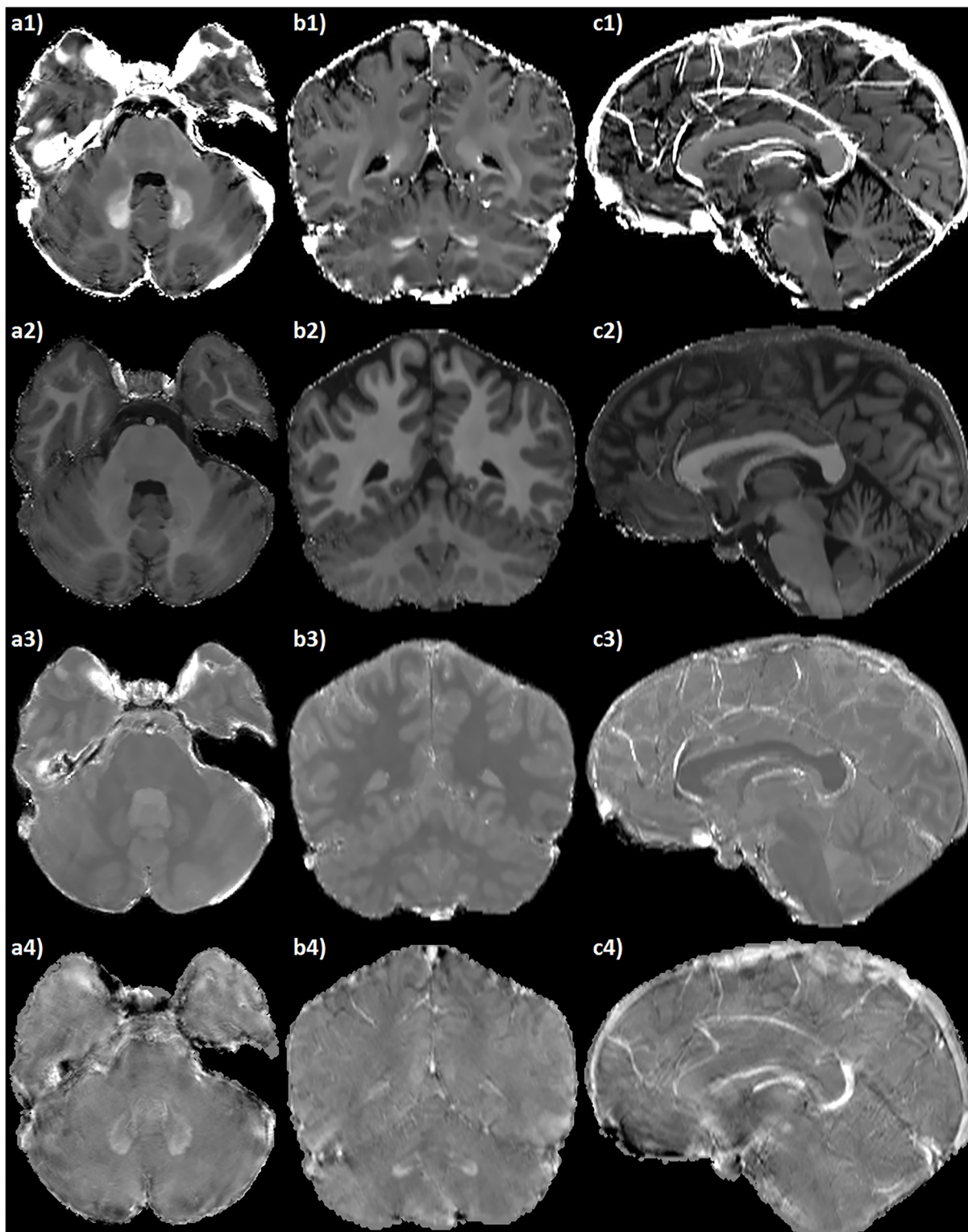
Fig 5. Multi-planar reconstructions of the RESUME maps. Axial (a), coronal (b) and sagittal (c) brain slices of: 1) R_2^* map ($[0 \sim 50]$ s^{-1}); 2) R_1 map ($[0 \sim 2]$ s^{-1}); 3) PD map ($[0 \sim 1]$ arbitrary units); 4) QSM ($[-300 \sim 300] \cdot 10^{-9}$) maps. The axial and coronal slices are centered at the level of the cerebellar dentate nuclei (remarkably conspicuous in the R_2^* and QSM maps due to their increased iron content); the sagittal slice is centered on the midline, where the deoxyhemoglobin-rich intracranial veins are particularly evident in the R_2^* and QSM maps.

https://doi.org/10.1371/journal.pone.0189933.g005
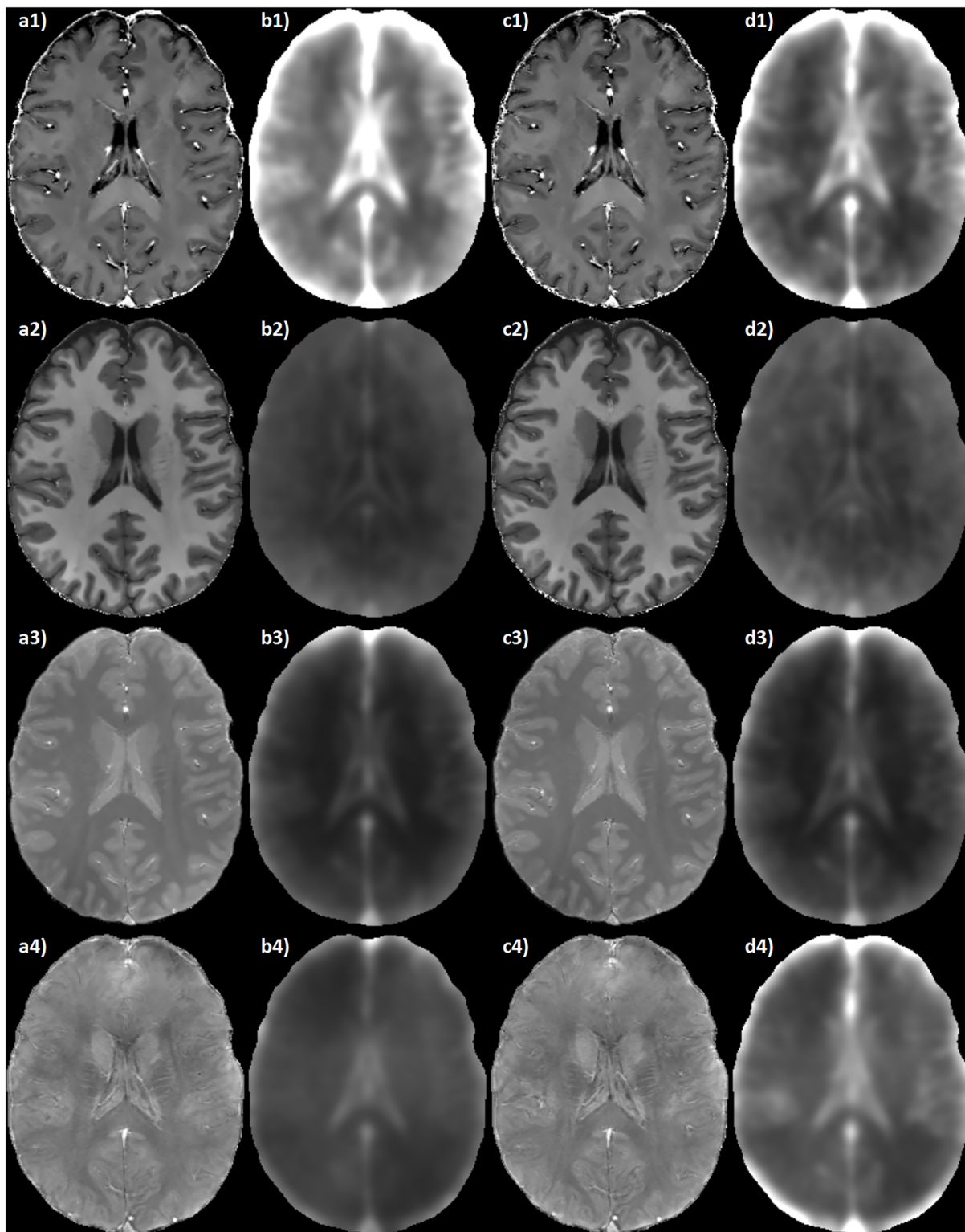
Fig 6. Reproducibility and accuracy of the RESUME maps. From left to right: a) RESUME maps of the spatial reference (HC1); b) voxelwise average, in the pool of subjects, of the $\{\sigma_j(\vec{x})\}$ maps spatially normalized to HC1; c) qMRI reference maps of HC1 obtained following [16] (for R_2^*, R_1 and PD maps) and from the 8-echo GRE (for the QSM); d) voxelwise average, in the pool of subjects, of the $\{\delta_j(\vec{x})\}$ maps spatially normalized to HC1. From top to bottom: 1) R_2^* map ([0 ∼ 50] s^{-1}); 2) R_1 map ([0 ∼ 2] s^{-1}); 3) PD map ([0 ∼ 1] arbitrary units); 4) QSM ([−300 ∼ 300] · 10^{-9}). Please note that the averages of $\{\sigma_j(\vec{x})\}$ (b) and $\{\delta_j(\vec{x})\}$ (d) are shown with an enhancement factor of 20.

https://doi.org/10.1371/journal.pone.0189933.g006

Table 1. Mean and standard deviation of the qMRI values in different brain regions, measured by RESUME or by the reference method [16] (Ref) in the healthy controls or found in the literature. PD values are normalized to the cerebrospinal fluid (CSF). Relaxometry values are compared with other 3D measures at 3 T.

	R_1 (s^{-1})	R_2^* (s^{-1})	PD (CSF)	QSM $\cdot 10^9$
White matter	1.08 ± 0.10	21.1 ± 1.1	0.718 ± 0.015	−5 ± 10
	1.07 ± 0.11 (Ref)	21.2 ± 1.2 (Ref)	0.699 ± 0.016 (Ref)	−2 ± 13 (Ref)
	1.036 ± 0.036 [39]	21.0 ± 0.8 [39]	0.742 ± 0.070 [39]	−18 ± 9 [40]
	1.190 ± 0.071 [41]		0.683 ± 0.006 [42]	
Cortical grey matter	0.624 ± 0.032	15.1 ± 1.6	0.852 ± 0.037	23 ± 30
	0.603 ± 0.045 (Ref)	14.6 ± 1.9 (Ref)	0.840 ± 0.043 (Ref)	21 ± 27 (Ref)
	0.609 ± 0.008 [39]	15.2 ± 0.4 [39]	0.796 ± 0.078 [39]	16 ± 10 [40]
	0.622 ± 0.043 [41]		0.844 ± 0.019 [42]	
Head of caudate nucleus	0.625 ± 0.054	20.2 ± 1.6	0.883 ± 0.019	68 ± 31
	0.615 ± 0.046 (Ref)	19.5 ± 1.4 (Ref)	0.860 ± 0.039 (Ref)	66 ± 29 (Ref)
	0.683 ± 0.022 [39]	18.2 ± 1.2 [39]	0.851 ± 0.084 [39]	60 ± 30 [43]
	0.719 ± 0.025 [41]		0.827 ± 0.016 [42]	78 ± 32 [44]
Putamen	0.663 ± 0.052	23.0 ± 2.0	0.886 ± 0.013	29 ± 16
	0.656 ± 0.051 (Ref)	22.8 ± 1.2 (Ref)	0.865 ± 0.018 (Ref)	30 ± 15 (Ref)
	0.752 ± 0.040 [41]	30.6 ± 4.7 [45]		70 ± 20 [40]
	0.70 ± 0.05 [46]			40 ± 20 [43]

parameters that could both increase the sensitivity of clinical MR scans, thus providing unique information about brain pathophysiology, and simplify the data harmonization in longitudinal or multicentric studies.

However, despite the growing interest of the neuroimaging community for qMRI (which provides hints on longitudinal and transverse relaxation processes, spin density, magnetic susceptibility, etc.), a certain skepticism usually creeps up at the moment of designing an acquisition protocol that could include it, for three main reasons.

First, the total acquisition time of a qMRI protocol that yields adequate resolution and SNR maps may be disheartening: in [47, 48], R_1 and R_2 maps (neglecting susceptibility phenomena and PD) were obtained in about 15 minutes, while the method described in [16] squeezed in the same duration a complete high-resolution qMRI scheme; conversely, other authors succeeded in lowering the acquisition time (in the order of 5 minutes), but they greatly sacrificed the resolution ([49, 50] stooped to a slice thickness of 5 mm).

Second, the sequences required by the great majority of the qMRI approaches are usually of poor radiological relevance as source of traditional MR image contrasts: in a clinical context, for instance, a T_2-weighted Fast Spin Echo (FSE) is commonly preferred to the TrueFISP [16, 51, 52]; a Magnetization-Prepared RApid Gradient-Echo (MPRAGE) or T_1-weighted SE are usually acquired instead of short T_E-GRE; a PD-weighted FSE, if necessary, substitutes the low FA-GRE [42, 48]; etc.

Last but not least, the search for efficient or accurate qMRI protocols often leads to the development of prototype sequences [49, 50, 53] that are, as such, rarely available if not exclusive of the developing research center.

RESUME scheme reverses the situation, being based on a clinical sequence that leads to the widespread SWI processing, thus exploiting an acquisition time that is usually accorded in a protocol design. Given that the standard SWI reconstruction is provided, the RESUME approach allows for an additional reconstruction of a complete set of qMRI maps (R_1, R_2^*, PD
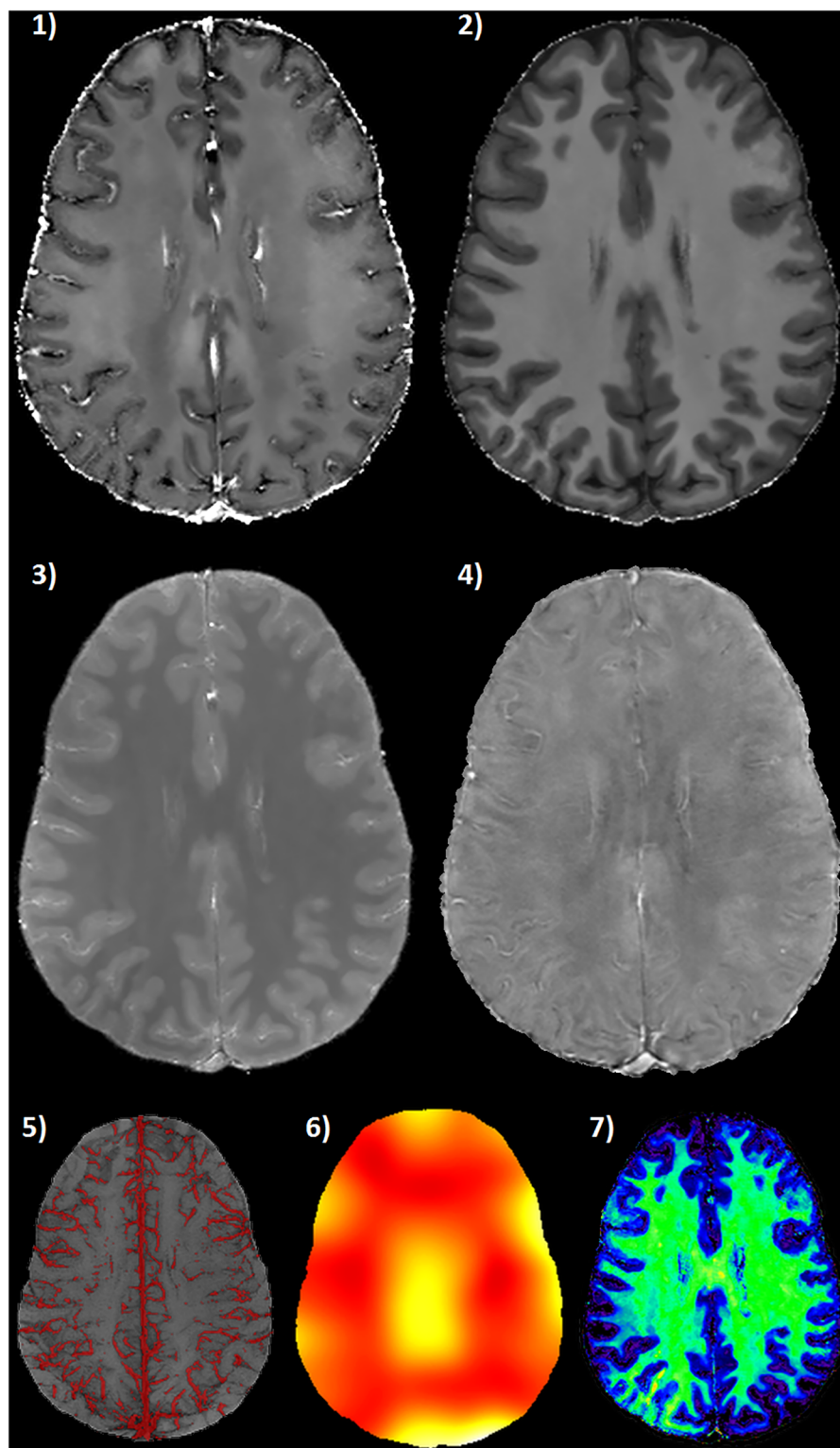
Fig 7. Extended qMRI processing of the RESUME protocol. Axial brain slices of: 1) R_2^* map ([$0 \sim 50$] s^{-1}); 2) R_1 map ([$0 \sim 2$] s^{-1}); 3) PD map ([$0 \sim 1$] arbitrary units); 4) QSM ([$-300 \sim 300$] $\cdot 10^{-9}$); 5) MAVEN vein segmentation; 6) OEF map ([$0 \sim 0.4$]); 7) MTVF map ([$0 \sim 0.5$]). MAVEN segmentation is Maximum-Intensity-Projected on a slab thickness of 20 mm and fused on the minimum-Intensity-Projection of the corresponding SWI slab (computed from the second echo of the dual-echo GRE), which serves as anatomical reference.

https://doi.org/10.1371/journal.pone.0189933.g007

and QSM) at the cost of a 50% additional acquisition time (typically in the order of 2 minutes for high-resolution SWI).

The derived maps share the same resolution of the SWI, thus being suitable for multi-planar reconstructions (see Fig 5) and for the study of thin structures such as the cortex, small gray matter nuclei and medullary veins (see Figs 4 and 7).

Despite the short acquisition time (overall protocol duration of ~ 7 minutes), the derived qMRI datasets exhibit a considerably high SNR even at a simple visual inspection. This is further confirmed by the confidence interval maps (see Fig 6), whose extent encompasses general reproducibility aspects besides the phenomena strictly connected to noise propagation.

A comparison with the maps obtained by an established state-of-the-art qMRI protocol [16] highlights an excellent accuracy of the RESUME results: indeed, the magnitude of the difference between the values estimated by the two methods falls within the limits fixed by the reproducibility issues. Moreover, the ranges of RESUME measures in different brain structures of HCs are consistent with those found in the literature for a variety of different qMRI approaches (see Table 1).

In this context, it is worth stressing the 3D nature of the acquired sequences that lead to the estimation of the relaxation parameters. Indeed, as most clearly pointed out in [32], relaxometry schemes based on 2D imaging sequences are prone to severe and barely rectifiable inaccuracies, due to the intrinsic intra-voxel FA variations of the slice-selective RF pulses. Furthermore, a comparison of Inversion Recovery (IR)-based T_1-mapping schemes [41] showed that 2D multislice acquisitions, such as IR-FSE, lead to an underestimation of T_1, due to several source of errors (such as flow, perfusion, through-plane motion, magnetization transfer caused by off-resonance excitation, non-ideal slice profiles, etc.) that are much less relevant on 3D sequences. On the other hand, relaxometry from 3D sequences can easily include B_1-inhomogeneity correction schemes, $e.g.$ based on the acquisition of the B_1-map, and this seems consistent with the substantial agreement of the longitudinal relaxation rates measured in several brain structures by RESUME and by multiple MPRAGEs acquired at different inversion times [41].

From a computational point of view, the analytical RESUME solutions for the relaxometry equations are particularly beneficial for the processing execution time: the negligible burden associated with the computation of Eqs 4, 21 and 23 allows for an inexpensive application of the iterative B_1-inhomogeneity correction adopted, so that the denoising step remains the bottleneck of an acceptable 10-minutes pipeline.

Finally, the interest in acquiring a thorough qMRI protocol like RESUME may also go beyond the extraction of classical relaxometry or susceptibility maps. In fact, the reconstructed parameters allow for additional quantitative processing steps that rely on the primary RESUME maps, such as the vessel-based analyses leading to vein segmentation and OEF maps, or the assessment of macromolecule density and local physico-chemical environment (see Fig 7).

In conclusion, the proposed acquisition and processing scheme allows for an accurate, reproducible and time-affordable strategy for obtaining different quantitative measures from a brain MRI scan. These features make RESUME feasible not only for research aims, but also for clinical practice, in light of an always increasing incorporation of qMRI protocols in the neuro-radiological routine.

Author Contributions

Conceptualization: Giuseppe Palma.

Data curation: Pasquale Borrelli, Sirio Cocozza.

Formal analysis: Giuseppe Palma.

Methodology: Giuseppe Palma.

Software: Pasquale Borrelli, Giuseppe Palma.

Supervision: Giuseppe Palma.

Validation: Giuseppe Palma.

Writing – original draft: Serena Monti, Giuseppe Palma.

Writing – review & editing: Serena Monti, Enrico Tedeschi, Sirio Cocozza, Giuseppe Palma.

References

1. Haacke EM, Reichenbach JR. Susceptibility weighted imaging in MRI: basic concepts and clinical applications. John Wiley & Sons; 2014.

2. Haacke EM, Xu Y, Cheng YCN, Reichenbach JR. Susceptibility weighted imaging (SWI). Magnetic resonance in medicine. 2004; 52(3):612–618. https://doi.org/10.1002/mrm.20198 PMID: 15334582

3. Schweser F, Deistung A, Lehr BW, Reichenbach JR. Differentiation between diamagnetic and paramagnetic cerebral lesions based on magnetic susceptibility mapping. Medical physics. 2010; 37 (10):5165–5178. https://doi.org/10.1118/1.3481505 PMID: 21089750

4. Lee J, Shmueli K, Kang BT, Yao B, Fukunaga M, van Gelderen P, et al. The contribution of myelin to magnetic susceptibility-weighted contrasts in high-field MRI of the brain. Neuroimage. 2012; 59 (4):3967–3975. https://doi.org/10.1016/j.neuroimage.2011.10.076 PMID: 22056461

5. Cerdonio M, Congiu-Castellano A, Mogno F, Pispisa B, Romani G, Vitale S. Magnetic properties of oxyhemoglobin. Proceedings of the National Academy of Sciences. 1977; 74(2):398–400. https://doi.org/10.1073/pnas.74.2.398

6. Mittal S, Wu Z, Neelavalli J, Haacke EM. Susceptibility-weighted imaging: technical aspects and clinical applications, part 2. American Journal of neuroradiology. 2009; 30(2):232–252. https://doi.org/10.3174/ajnr.A1461 PMID: 19131406

7. Tong K, Ashwal S, Obenaus A, Nickerson J, Kido D, Haacke E. Susceptibility-weighted MR imaging: a review of clinical applications in children. American Journal of Neuroradiology. 2008; 29(1):9–17. https://doi.org/10.3174/ajnr.A0786 PMID: 17925363

8. Robinson RJ, Bhuta S. Susceptibility-Weighted Imaging of the Brain: Current Utility and Potential Applications. Journal of Neuroimaging. 2011; 21(4):e189–e204. https://doi.org/10.1111/j.1552-6569.2010.00516.x PMID: 21281380

9. Liu C, Li W, Tong KA, Yeom KW, Kuzminski S. Susceptibility-weighted imaging and quantitative susceptibility mapping in the brain. Journal of Magnetic Resonance Imaging. 2015; 42(1):23–41. https://doi.org/10.1002/jmri.24768 PMID: 25270052

10. Wu ML, Chang HC, Chao TC, Chen NK. Efficient imaging of midbrain nuclei using inverse double-echo steady-state acquisition. Medical physics. 2015; 42(7):4367–4374. https://doi.org/10.1118/1.4922402 PMID: 26133633

11. Ma YJ, Liu W, Zhao X, Tang W, Li H, Fan Y, et al. 3D interslab echo-shifted FLASH sequence for susceptibility weighted imaging. Magnetic resonance in medicine. 2015;.

12. Du J, Hamilton G, Takahashi A, Bydder M, Chung CB. Ultrashort echo time spectroscopic imaging (UTESI) of cortical bone. Magnetic resonance in medicine. 2007; 58(5):1001–1009. https://doi.org/10.1002/mrm.21397 PMID: 17969110

13. Holdsworth SJ, Yeom KW, Moseley ME, Skare S. Fast susceptibility-weighted imaging with three-dimensional short-axis propeller (SAP)-echo-planar imaging. Journal of Magnetic Resonance Imaging. 2015; 41(5):1447–1453. https://doi.org/10.1002/jmri.24675 PMID: 24956237

14. Schwarz ST, Afzal M, Morgan PS, Bajaj N, Gowland PA, Auer DP. The'Swallow Tail' Appearance of the Healthy Nigrosome—A New Accurate Test of Parkinson's Disease: A Case-Control and Retrospective Cross-Sectional MRI Study at 3T. PLoS One. 2014; 9(4):e93814. https://doi.org/10.1371/journal.pone.0093814 PMID: 24710392

15. Haacke EM, Mittal S, Wu Z, Neelavalli J, Cheng YC. Susceptibility-weighted imaging: technical aspects and clinical applications, part 1. American Journal of Neuroradiology. 2009; 30(1):19–30. https://doi.org/10.3174/ajnr.A1400 PMID: 19039041

16. Palma G, Tedeschi E, Borrelli P, Cocozza S, Russo C, Liu S, et al. A novel multiparametric approach to 3D quantitative MRI of the brain. PloS one. 2015; 10(8):e0134963. https://doi.org/10.1371/journal.pone.0134963 PMID: 26284778

17. Wang Y, Liu T. Quantitative susceptibility mapping (QSM): decoding MRI data for a tissue magnetic bio-marker. Magnetic resonance in medicine. 2015; 73(1):82–101. https://doi.org/10.1002/mrm.25358 PMID: 25044035

18. Liu C, Wei H, Gong NJ, Cronin M, Dibb R, Decker K. Quantitative Susceptibility Mapping: Contrast Mechanisms and Clinical Applications. Tomography: a journal for imaging research. 2015; 1(1):3. https://doi.org/10.18383/j.tom.2015.00136

19. Monti S, Palma G, Borrelli P, Tedeschi E, Cocozza S, Salvatore M, et al. A multiparametric and multi-scale approach to automated segmentation of brain veins. In: 2015 37th Annual International Conference of the IEEE Engineering in Medicine and Biology Society (EMBC). IEEE; 2015. p. 3041–3044.

20. Monti S, Cocozza S, Borrelli P, Straub S, Ladd ME, Salvatore M, et al. MAVEN: an Algorithm for Multi-Parametric Automated Segmentation of Brain Veins from Gradient Echo Acquisitions. IEEE Transactions on Medical Imaging. 2017; PP(99):1–1.

21. Hattingen E, Jurcoane A, Nelles M, Müller A, Nöth U, Mädler B, et al. Quantitative MR Imaging of Brain Tissue and Brain Pathologies. Clinical neuroradiology. 2015; 25(2):219–224. https://doi.org/10.1007/s00062-015-0433-8 PMID: 26223371

22. Draganski B, Ashburner J, Hutton C, Kherif F, Frackowiak RS, Helms G, et al. Regional specificity of MRI contrast parameter changes in normal ageing revealed by voxel-based quantification (VBQ). Neuroimage. 2011; 55(4):1423–1434. https://doi.org/10.1016/j.neuroimage.2011.01.052 PMID: 21277375

23. Sereno MI, Lutti A, Weiskopf N, Dick F. Mapping the human cortical surface by combining quantitative T1 with retinotopy. Cerebral Cortex. 2013; 23(9):2261–2268. https://doi.org/10.1093/cercor/bhs213 PMID: 22826609

24. Lutti A, Dick F, Sereno MI, Weiskopf N. Using high-resolution quantitative mapping of R1 as an index of cortical myelination. Neuroimage. 2014; 93:176–188. https://doi.org/10.1016/j.neuroimage.2013.06.005 PMID: 23756203

25. Komiyama M, Yagura H, Baba M, Yasui T, Hakuba A, Nishimura S, et al. MR imaging: possibility of tis-sue characterization of brain tumors using T1 and T2 values. American journal of neuroradiology. 1987; 8(1):65–70. PMID: 3028112

26. Just M, Thelen M. Tissue characterization with T1, T2, and proton density values: results in 160 patients with brain tumors. Radiology. 1988; 169(3):779–785. https://doi.org/10.1148/radiology.169.3.3187000 PMID: 3187000

27. Mezer A, Yeatman JD, Stikov N, Kay KN, Cho NJ, Dougherty RF, et al. Quantifying the local tissue volume and composition in individual brains with magnetic resonance imaging. Nature medicine. 2013; 19(12):1667–1672. https://doi.org/10.1038/nm.3390 PMID: 24185694

28. Allkemper T, Tombach B, Schwindt W, Kugel H, Schilling M, Debus O, et al. Acute and Subacute Intra-cerebral Hemorrhages: Comparison of MR Imaging at 1.5 and 3.0 T—Initial Experience 1. Radiology. 2004; 232(3):874–881. https://doi.org/10.1148/radiol.2323030322 PMID: 15284437

29. Tedeschi E, Palma G, Canna A, Cocozza S, Russo C, Borrelli P, et al. In vivo dentate nucleus MRI relaxometry correlates with previous administration of Gadolinium-based contrast agents. European radiology. 2016; p. 1–8.

30. Tedeschi E, Cocozza S, Borrelli P, Ugga L, Morra VB, Palma G. Longitudinal Assessment of Dentate Nuclei Relaxometry during Massive Gadobutrol Exposure. Magnetic Resonance in Medical Sciences. 2017;advpub. https://doi.org/10.2463/mrms.cr.2016-0137 PMID: 28367903

31. Cocozza S, Russo C, Pisani A, Olivo G, Riccio E, Cervo A, et al. Redefining the pulvinar sign in Fabry's disease. American Journal of Neuroradiology. 2017;In press. https://doi.org/10.3174/ajnr.A5420 PMID: 29051208

32. Brown RW, Cheng YCN, Haacke EM, Thompson MR, Venkatesan R. Magnetic resonance imaging: physical principles and sequence design. John Wiley & Sons; 2014.

33. Deistung A, Schweser F, Reichenbach JR. Overview of quantitative susceptibility mapping. NMR in Bio-medicine. 2016;.

34. Li W, Wang N, Yu F, Han H, Cao W, Romero R, et al. A method for estimating and removing streaking artifacts in quantitative susceptibility mapping. Neuroimage. 2015; 108:111–122. https://doi.org/10.1016/j.neuroimage.2014.12.043 PMID: 25536496

35. Borrelli P, Palma G, Comerci M, Alfano B. Unbiased noise estimation and denoising in parallel magnetic resonance imaging. In: Acoustics, Speech and Signal Processing (ICASSP), 2014 IEEE International Conference on. IEEE; 2014. p. 1230–1234.

36. Palma G, Comerci M, Alfano B, Cuomo S, De Michele P, Piccialli F, et al. 3D Non-Local Means denoising via multi-GPU. In: Computer Science and Information Systems (FedCSIS), 2013 Federated Conference on. IEEE; 2013. p. 495–498.

37. Borrelli P, Palma G, Tedeschi E, Cocozza S, Comerci M, Alfano B, et al. Improving Signal-to-Noise Ratio in Susceptibility Weighted Imaging: A Novel Multicomponent Non-Local Approach. PloS one. 2015; 10(6):e0126835. https://doi.org/10.1371/journal.pone.0126835 PMID: 26030293

38. Kudo K, Liu T, Murakami T, Goodwin J, Uwano I, Yamashita F, et al. Oxygen extraction fraction measurement using quantitative susceptibility mapping: comparison with positron emission tomography. Journal of Cerebral Blood Flow & Metabolism. 2016; 36(8):1424–1433. https://doi.org/10.1177/0271678X15606713

39. Warntjes JB, Engström M, Tisell A, Lundberg P. Brain characterization using normalized quantitative magnetic resonance imaging. PloS one. 2013; 8(8):e70864. https://doi.org/10.1371/journal.pone.0070864 PMID: 23940653

40. Schweser F, Deistung A, Lehr BW, Reichenbach JR. Quantitative imaging of intrinsic magnetic tissue properties using MRI signal phase: an approach to in vivo brain iron metabolism? Neuroimage. 2011; 54(4):2789–2807. https://doi.org/10.1016/j.neuroimage.2010.10.070 PMID: 21040794

41. Wright P, Mougin O, Totman J, Peters A, Brookes M, Coxon R, et al. Water proton T1 measurements in brain tissue at 7, 3, and 1.5 T using IR-EPI, IR-TSE, and MPRAGE: results and optimization. Magnetic Resonance Materials in Physics, Biology and Medicine. 2008; 21(1–2):121. https://doi.org/10.1007/s10334-008-0104-8

42. Weiskopf N, Suckling J, Williams G, Correia MM, Inkster B, Tait R, et al. Quantitative multi-parameter mapping of R1, PD*, MT, and R2* at 3T: a multi-center validation. Frontiers in neuroscience. 2013; 7:95. https://doi.org/10.3389/fnins.2013.00095 PMID: 23772204

43. Doganay S, Gumus K, Koc G, Bayram AK, Dogan MS, Arslan D, et al. Magnetic Susceptibility Changes in the Basal Ganglia and Brain Stem of Patients with Wilson's Disease: Evaluation with Quantitative Susceptibility Mapping. Magnetic Resonance in Medical Sciences. 2017; p. https://doi.org/10.2463/mrms.mp.2016-0145 PMID: 28515413

44. Langkammer C, Schweser F, Krebs N, Deistung A, Goessler W, Scheurer E, et al. Quantitative susceptibility mapping (QSM) as a means to measure brain iron? A post mortem validation study. Neuroimage. 2012; 62(3):1593–1599. https://doi.org/10.1016/j.neuroimage.2012.05.049 PMID: 22634862

45. Yan SQ, Sun JZ, Yan YQ, Wang H, Lou M. Evaluation of brain iron content based on magnetic resonance imaging (MRI): comparison among phase value, R2* and magnitude signal intensity. PloS one. 2012; 7(2):e31748. https://doi.org/10.1371/journal.pone.0031748 PMID: 22363719

46. Lee EY, Flynn MR, Du G, Lewis MM, Fry R, Herring AH, et al. T1 relaxation rate (R1) indicates nonlinear Mn accumulation in brain tissue of welders with low-level exposure. Toxicological Sciences. 2015; 146 (2):281–289. https://doi.org/10.1093/toxsci/kfv088 PMID: 25953701

47. Deoni SC, Rutt BK, Peters TM. Rapid combined T1 and T2 mapping using gradient recalled acquisition in the steady state. Magnetic Resonance in Medicine. 2003; 49(3):515–526. https://doi.org/10.1002/mrm.10407 PMID: 12594755

48. Deoni SC, Peters TM, Rutt BK. High-resolution T1 and T2 mapping of the brain in a clinically acceptable time with DESPOT1 and DESPOT2. Magnetic resonance in medicine. 2005; 53(1):237–241. https://doi.org/10.1002/mrm.20314 PMID: 15690526

49. Warntjes J, Leinhard OD, West J, Lundberg P. Rapid magnetic resonance quantification on the brain: Optimization for clinical usage. Magnetic Resonance in Medicine. 2008; 60(2):320–329. https://doi.org/10.1002/mrm.21635 PMID: 18666127

50. West J, Warntjes J, Lundberg P. Novel whole brain segmentation and volume estimation using quantitative MRI. European radiology. 2012; 22(5):998–1007. https://doi.org/10.1007/s00330-011-2336-7 PMID: 22113264

51. Deoni SC, Rutt BK, Arun T, Pierpaoli C, Jones DK. Gleaning multicomponent T1 and T2 information from steady-state imaging data. Magnetic Resonance in Medicine. 2008; 60(6):1372–1387. https://doi.org/10.1002/mrm.21704 PMID: 19025904

52. Deoni SC. Transverse relaxation time (T2) mapping in the brain with off-resonance correction using phase-cycled steady-state free precession imaging. Journal of Magnetic Resonance Imaging. 2009; 30 (2):411–417. https://doi.org/10.1002/jmri.21849 PMID: 19629970

53. Metere R, Kober T, Möller HE, Schäfer A. Simultaneous Quantitative MRI Mapping of T1, T2* and Magnetic Susceptibility with Multi-Echo MP2RAGE. PloS one. 2017; 12(1):e0169265. https://doi.org/10.1371/journal.pone.0169265 PMID: 28081157